Ocean Engineering 315 (2025) 119917

Contents lists available at ScienceDirect

Ocean Engineering

journal homepage: www.elsevier.com/locate/oceaneng

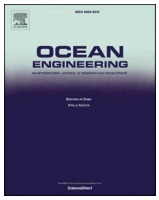

Research paper

Improving the power production of Mutriku Wave Power Plant throughout tuning the actual generator and damping valve limits

Joseba Lopez-Mendia [a,b,*], Ander Aristondo [a,c], Pierpaolo Ricci [d], Jon Lekube [e], Salvador Ceballos [a,f], Eider Robles [a,b]

[a] TECNALIA, Basque Research and Technology Alliance (BRTA), Parque Tecnológico de Bizkaia, Astondo Bidea, Edificio 700, E-48160, Derio, Spain
[b] Automatics and System Engineering Department, University of the Basque Country UPV/EHU, Bilbao, 48013, Spain
[c] Fluid Mechanics Department. Mondragon University, Arrasate, Spain
[d] SSE Renewables, 1 Forbury Place, Forbury Road. Reading, RG1 3JH, United Kingdom
[e] Biscay Marine Energy Platform—BiMEP, Atalaia 2 bajo, 48620, Armintza, Spain
[f] Department of Electronics Technology, University of the Basque Country UPV/EHU, Bilbao, 48013, Spain

ARTICLE INFO

Keywords:
Mutriku wave power plant
Wave energy converters
Oscillating water column
Power take-off
Induction generator

ABSTRACT

The Mutriku Wave Power Plant (MWPP) has successfully operated since 2011, demonstrating remarkable operational stability with minimal issues of OWC technology in breakwaters. So far, the design, selection, and operation ranges of the generators at MWPP prioritized reliability. However, once the viability of the technology has been demonstrated, it is important to explore ways to increase energy production with the current design of the technology.

The objective of the present work is to improve the power production in MWPP throughout the Power take-off (PTO), increasing the operational limits of the generator and of the damping valve, which is located between the air chamber and the turbine. To this aim, new sensors have been installed in the plant, such as an inlet pressure sensor, to characterise the behaviour of the PTO. Investigations into the power produced and the plant availability have concluded that modifying control laws of the current configuration could help to increase power production under generator thermal operation ranges.

The numerical results presented in the paper demonstrate that the potential benefit to the overall energy production of the MWPP could be significant, leading to greater advancements in the feasibility of wave energy technologies. The analysis of changes and improvements into the MWPP control strategies will provide further guidance into the development of novel wave energy control systems and components for future testing.

Nomenclature

OWC	Oscillating Water Column
B2B	Back to Back
EU	Europe
IWS	Internal Water Surface
MSL	Mean Sea Level
MW	Megawatt
MLWS	Mean Low Water Springs
MWPP	Mutriku Wave Power Plant
PTO	Power Take-Off
rms	Root Mean Square
WEC	Wave Energy Converter

1. Introduction

Deploying Oscillating Water Column (OWC) technology within breakwaters to install wave energy converters (WECs) offers a compelling and effective solution for tapping into renewable energy derived from ocean waves (Xu and Huang, 2018), (Scialò et al., 2021), (Fox et al., 2021). Moreover, OWC represents one of the most developed WEC concepts (Falcão and Henriques, 2016). OWC devices fall into two main categories: fixed, typically attached to the seabed or shoreline, such as MWPP (Faÿ et al., 2020a), Pico wave power plant (Falcão et al., 2020) or Limpet (Heath, 2000), and floating devices, not fixed to a specific location, allowing them to be deployed in deeper waters, such as IDOM-Marmok spar-type buoy (Touzon et al., 2018), OE buoy

* Corresponding author. Automatics and System Engineering Department, University of the Basque Country UPV/EHU, Bilbao, 48013, Spain.
E-mail address: joseba.lopez@tecnalia.com (J. Lopez-Mendia).

https://doi.org/10.1016/j.oceaneng.2024.119917
Received 5 September 2024; Received in revised form 12 November 2024; Accepted 24 November 2024
Available online 28 November 2024

(WEDUSEA wave energy project) or Wave swell (Wave Swell). The present study will focus on the improvement of MWPP power production, located in Mutriku (Torre-Enciso et al., 2009), a town in the Basque Country, North of Spain. MWPP is one of the firsts commercial wave power plants in the world (Fig. 1) and one of the very few still operational and continuously active since its commissioning.

Inaugurated in 2011, the development was partially supported by the NEREIDA MOWC project (Nereida) and executed by the Basque Energy Agency (Homea). This commercial facility continuously generates electricity by harnessing the energy generated by the waves. The generated energy is seamlessly fed into the grid, equivalent to the annual consumption of approximately one hundred households. Consequently, it stands as the world's longest-standing wave energy plant, having produced and supplied the highest amount of energy to the grid. Furthermore, it boasts the highest accumulated operational hours and availability. In 2016, marking its fifth anniversary, MWPP reached the significant milestone of being the world's first facility of its kind to produce 1 GWh of energy. 2020 set a new production record (Mutriku Wave Energy Plant hits) by reaching an accumulated 2 GWh, and 3 GWh in 2024 (The Mutriku wave plant achieves), a generation milestone never before achieved in a facility harnessing wave energy to produce electricity.

It's worth noting that the MWPP serves not only as an energy-generating facility but also as a demonstration project that provides valuable insights into the feasibility and efficiency of wave energy conversion technologies. MWPP has served as a study basis for the improvement of OWC PTOs, such as the OPERA H2020 European project (Homeb), where a biradial turbine was tested (Gato et al., 2022), as well as advanced controllers to maximize power extraction (Faÿ et al., 2020b), (Faÿ et al., 2020c), (Carrelhas et al., 2023). Other studies such as (Lekube et al., 2018a) also focus research on the control of MWPP. MWPP consists of 16 OWC air chambers designed to produce pneumatic pressure fluctuations, initiating a bidirectional oscillating airflow through the turbine. All chambers share identical dimensions, measuring 3.1 m in length, and 4.5 m in width oriented to face directly towards the incoming waves, and the turbine positioned 9.7 m above the Mean Low Water Springs (MLWS) level. Fig. 2 presents a turbine gallery lay-out:

The oscillating air movement within the chamber is channelled through a turbine located at the top of the structure. The turbine is connected to a generator, and as the air flows back and forth, it makes the turbine spin, converting mechanical energy into electricity. The generated electricity is then fed into the grid for distribution and use. The plant contributes renewable energy to the local power supply without emitting greenhouse gases during the generation process.

The Wells turbine, which consists of co-rotating double monoplanes, rotates in the same direction irrespective of the airflow orientation, owing to its inherent self-rectifying nature. The turbine, featuring a 5-bladed design with a diameter of 0.75 m, is mechanically coupled to an 18.5 kW induction generator equipped with a squirrel-cage rotor. The generator operates at a voltage of 460 V and a nominal speed of 3,000 rpm.

Facilitating variable speed operation, the generated power initially undergoes conversion to direct current (DC) and subsequently transitions to alternating current (AC) with a consistent frequency and phase matching the power supply grid (50 Hz). To achieve this, each generator is linked to a variable-frequency drive, which serves the dual purpose of rectification and primary control over the turbo-generator. A unique configuration involves two groups of eight variable frequency drives, one per each turbo-generator, organized within a 700 V DC-link, utilizing a singular regenerative inverter drive for each group to convert DC to AC. The resulting power is then transmitted through the output power transformer at a voltage of 13.5 kV.

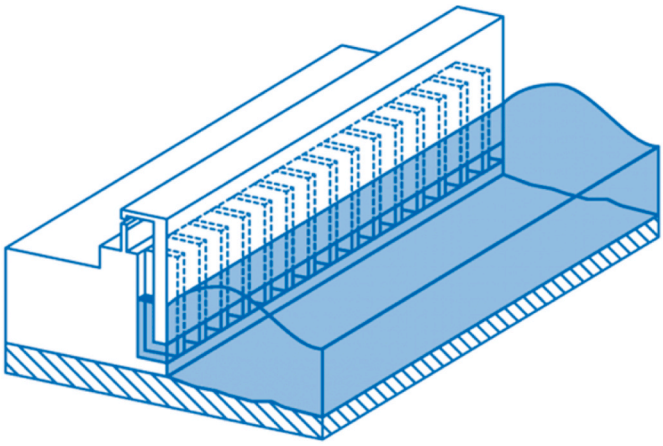

Fig. 2. MWPP turbine gallery layout (Características técnicas).

After having demonstrated the feasibility of the technology, one important objective for future development is increasing the energy production using the existing design. The goal of this work is to show how to enhance power output in the MWPP by optimizing the Power Take-Off (PTO) system, including the generator and the damping valve between the air chamber and turbine. To this aim, two strategies have been considered in this study.

- Increasing the Torque Limit: Since the stator winding failure is not a reported issue in MWPP (Lekube et al., 2018b)- (M'zoughi et al., 2024), it's feasible to consider increasing the generator's operating limits. This approach relies on previous studies (Lopez-Mendia et al., 2024), where the generator's behaviour during overload was examined. As long as the stator winding temperature remains well below the maximum allowable limit defined by the generator's insulation class, the torque limit of the generator can be extended. This allows the generator to manage higher loads, thereby potentially extracting more power.
- Adjusting the Damping Valve: The damping valve controls the available pneumatic input power at the turbine. It operates within a specific range of chamber pressure rms, from 5,250Pa to 15,250Pa. The angle of the valve changes depending on the moving average chamber pressure rms. By fine-tuning this valve, the pneumatic input

Fig. 1. Mutriku Wave Power Plant picture (Technical Characteristics).

power can be optimized, which in turn, could lead to an increase in power output.

These options aim to push the operational boundaries of the generator and the turbine system, thereby maximizing power extraction. However, it's important to monitor the system closely during these adjustments to prevent any potential damage or inefficiencies.

The paper is structured as follows: An overview of MWPP is presented in Section 1. Section 2 outlines the development of a multi-physics numerical model aimed at assessing MWPP performance. This model accurately estimates the produced power and the evolution of the generator's stator winding temperature, enabling performance prediction and monitoring under overload conditions. Section 3 builds on these results to explore the control laws for the generator and damping valve, with the goal of increasing the energy production. It also compares power production across several operational limits of the generator. Finally, Section 4 presents the conclusions and future work.

2. MWPP numerical model

This section describes the MWPP numerical model developed to analyse the capability of generator and damping valve limits to increase power production. Starting with a general description of the dynamics of the wave energy converter, the air chamber, the frequency domain model, and the PTO consisting of the Wells turbine, damping valve, and the generator will be presented, including a discussion on the thermal model for the generator to analyse its thermal limits. Fig. 3 represents the summary of the power conversion chain.

2.1. Dynamics of the oscillating water column

Given the dimensions of the chamber in comparison with the typical waves occurring at Mutriku, the free surface within the OWC chamber, hereafter referred to as the Internal Water Surface (IWS), is assumed to move as a weightless piston only capable of vertical displacement, because the wavelengths are large enough to neglect the influence of standing wave modes along the IWS. Therefore, the dynamics of the oscillating water column (Fig. 4) have been modelled through the dynamic equilibrium of forces acting on the water column IWS:

$$M\ddot{z}(t) = F_E(t) + F_R(t) + F_H(t) + F_{PTO}(t) \tag{1}$$

Where M represents the mass of rigid water piston, $\ddot{z}(t)$ denotes the acceleration of the free surface of the oscillating water column, $F_E(t)$ is the excitation force due to the waves, $F_R(t)$ is the radiation force, $F_H(t)$ is the hydrostatic force, and $F_{PTO}(t)$ is the force attributed to the presence of the Power Take-Off (PTO). The calculation of $F_E(t)$, and $F_R(t)$ depends on hydrodynamic coefficients that, in the frequency domain, represent the interaction between the IWS and the waves. For the calculation of $F_E(t)$, the excitation force coefficient in the frequency domain, $F_E(\omega)$, is employed. $F_E(\omega)$ represents the excitation force associated with an incident wave of frequency ω and an amplitude of 1 m. Typically, there are three positions to represent the mean sea level (MSL), at low tide, mean tide and high tide. For the present study, the mean tide has been considered (MSL = 2.77 m):

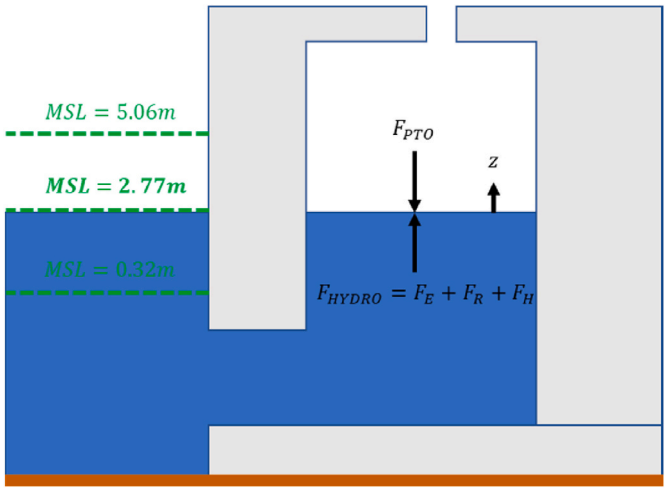

Fig. 4. Chamber of MWPP, and water levels: low tide, high tide, and mean tide.

The total excitation force in the time-domain for realistic irregular wave conditions (the sea states have been defined by the JONSWAP spectrum) can therefore be described as the superposition of N components associated with N waves with different frequencies:

$$F_E(t) = \sum_{j=1}^{N} F_E(\omega_j) a_j(\omega_j) \cos(\omega_j t + \varphi_j + \varepsilon_j) \tag{2}$$

The radiation force originates from the motion of the IWS. This force is computed as the sum of two terms. The first term, known as added mass, is an inertia term representing the force caused by the acceleration resulting from the movement of the IWS in the adjacent fluid. The second term is called radiation damping, and it represents the transfer of energy from the IWS to the medium due to the ripples generated by its oscillatory motion and radiated away from the chamber (Perez and Fossen, 2009).

$$F_R(t) = F_A(t) + F_{RAD}(t) = -A_\infty \ddot{z}(t) - \int_{-\infty}^{t} K_R(t-\tau)\dot{z}(\tau)d\tau \tag{3}$$

Where A_∞ is the added mass at infinite frequency (5), which can be derived from the added mass coefficient $A(\omega)$ in the frequency domain computed by standard commercial software and $K_R(t)$ is the impulse response function (4), which is calculated with the damping coefficients in the frequency domain, $B(\omega)$, using the equations:

$$K_R(t) = \frac{2}{\pi}\int_0^\infty B(\omega)\cos(\omega t)d\omega \tag{4}$$

$$A_\infty = A(\omega) + \frac{1}{\omega}\int_0^\infty K_R(t)\sin(\omega t)d\omega \tag{5}$$

In this work, the convolution integral used for the calculation of radia-

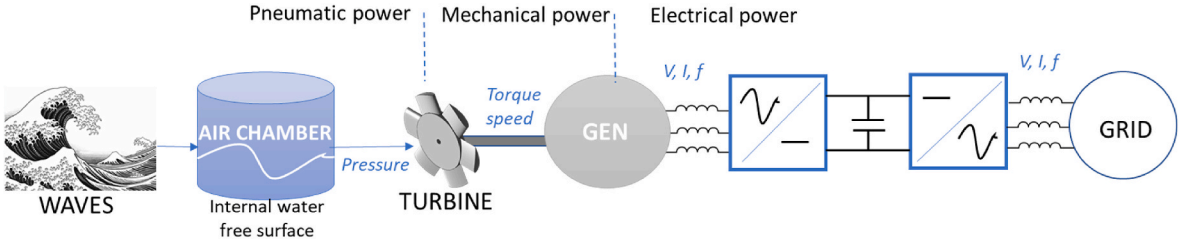

Fig. 3. Power conversion chain of an OWC device (Lopez-Mendia et al., 2024).

tion damping (3) has been approximated using the Prony (Duclos et al., 2001) method (6), enabling the approximation of radiation damping through the state-space representation shown in (7).

$$K_R(t) \approx \sum_{i=1}^{N} \alpha_i \, e^{\beta_i t} = \sum_{i=1}^{N} I_i \tag{6}$$

$$\begin{aligned} \dot{I}_i &= A_r I_i + B_r \dot{z} \\ F_{RAD} &= C_r I_i + D_r \dot{z} \end{aligned} \tag{7}$$

Where α_i y β_i are the Prony fitting coefficients, and A_r, B_r, C_r, D_r are the state-space matrices obtained from the Prony coefficients.

The hydrostatic force is proportional to the weight of water displaced during the oscillation of the free surface and is calculated as:

$$F_H(t) = -\rho_{H_2O} g S_{IWS} z(t) \tag{8}$$

Where ρ_{H_2O} is the density of water, g is the gravitational acceleration, and S_{IWS} is the area of the Internal Water Surface (IWS).

Finally, $F_{PTO}(t)$ is the force exerted by the PTO system and is proportional to the pressure difference between the interior of the air chamber and the environment outside the chamber. Assuming that the surroundings are at atmospheric pressure, $F_{PTO}(t)$ is computed as:

$$F_{PTO}(t) = -[p(t) - p_{atm}] \, S_{IWS} \tag{9}$$

Where $p(t)$ is the pressure inside the chamber, whose dynamics, introduced in Section 2.2, are described by (16), and p_{atm} is the atmospheric pressure.

2.2. Air chamber

Considering the relatively short time scales involved in the process, the compression and expansion of air within the chamber can be assumed to be adiabatic and modelled as an isentropic process, with physical air properties following the well understood laws of thermodynamics (Weber, 2007) for ideal gases. Under this assumption, the following relationship is derived:

$$\frac{p + p_{atm}}{\rho^{\gamma}} = \frac{p_{atm}}{\rho_{atm}^{\gamma}} \tag{10}$$

Where ρ is the density of air within the chamber, ρ_{atm} is the density of air at atmospheric pressure, p is the relative pressure in the chamber, γ is the isentropic expansion factor of air, which is assumed to be constant and equal to 1.4. For a better accuracy in the resolution of thermodynamic processes, usually the dimensionless pressure $p^* = p / p_{atm}$, Equation (10) can be rewritten as:

$$\frac{1}{\rho} = \frac{(p^* + 1)^{-\frac{1}{\gamma}}}{\rho_{atm}} \tag{11}$$

By differentiating (11) concerning time, we obtain:

$$\frac{\dot{\rho}}{\rho} = \frac{\dot{p^*}}{\gamma(p^* + 1)} \tag{12}$$

As the dimensionless coefficients defining the aerodynamic behaviour of the turbine are based on the flow rate, it is necessary to rewrite Equation (12) in terms of mass flow rate. Knowing that the mass flow rate across the turbine is defined as:

$$\dot{m} = \frac{d}{dt}(-\rho V) = -\rho \dot{V} - \dot{\rho} V \tag{13}$$

$$\dot{V} + \frac{\dot{\rho}}{\rho} V = -\frac{\dot{m}}{\rho} \tag{14}$$

Where $V = S_{IWS} \cdot (h_{ch} - z)$ is the volume of air in the chamber. Replacing the equations, we deduce that the time derivative of dimensionless pressure is:

$$\dot{z} S_{IWS} + \frac{\dot{p^*}}{\gamma(p^* + 1)} (h_{ch} - z) S_{IWS} = -\frac{\dot{m}}{\rho_{atm}} (p^* + 1)^{-\frac{1}{\gamma}} \tag{15}$$

Finally, after simplification the pressure evolution in the chamber is found to be:

$$\dot{p^*} = -\frac{\dot{m} \, \gamma \frac{p_{atm}}{\rho_{atm}}}{p_{atm} S_{IWS} (h_{ch} - z)} (p^* + 1)^{\frac{\gamma - 1}{\gamma}} - \gamma \frac{\dot{z}}{h_{ch} - z} (p^* + 1) \tag{16}$$

2.3. Frequency-domain model

The hydrodynamic modeling of OWCs is typically based on the assumptions of linear wave theory, also known as linear potential theory which assumes that the flow is incompressible and irrotational, with wave amplitudes and device displacements being small in comparison to the wavelength (Rosati et al., 2022a).

The frequency-domain analysis employs a boundary element method solver based on potential flow theory, specifically applied to the OWC chamber geometry of the plant situated along the seabed slope in front of the breakwater wall. Adopting the rigid piston modeling approach from previous work on the onshore OWC at Pico (Heath, 2000), the Internal Water Free Surface (IWFS) is treated as a massless oscillating body restricted to heave motion, with the chamber wall serving as the second fixed body.

For the MWPP, in the absence of detailed bathymetric data, the seabed geometry is simplified to a constant slope initiating 50 m ahead of the plant with a water depth of 15 m as presented in Fig. 5 (Faÿ et al., 2020d). The dyke's total length is set at 100 m positioning air chamber 9 at the center, a choice that aligns with the realistic layout of the actual plant.

Fig. 6 shows the hydrodynamic coefficients for the excitation force $F_E(t)$, radiation force $F_R(t)$, and added mass $A(\omega)$ over a range of frequencies between 0 rad/s and 1.8 rad/s, as derived from the hydrodynamic solver. Note that, at large frequencies, the value of the added mass tends to the added mass at infinite frequency $A(\infty)$ introduced before in the time-domain equation. The numerical model has been developed with the following hydrodynamic coefficients represented in Fig. 6:

2.4. Power Take-Off

The present study will focus on the behaviour of the Power Take-off (PTO) which consists of a Wells Turbine, damping valve, generator (SCIG 18.5 kW) and Back-to-back (B2B) converter (Unidrive SP2404 (Control Techniques Drives Limited, 2008)). The MWPP PTO (Fig. 7) attains maximum dimensions of 2.83 m in height, 1.25 m in width, and an estimated weight of 1200 kg. Consequently, assembly and disassembly procedures are uncomplicated, allowing for seamless execution in a singular piece.

2.4.1. Wells Turbine

The Wells turbine type (invented by Dr. Allan Wells in the mid-1970s (Raghunathan et al., 1982)), which is one of the most efficient OWC technologies (Shehata et al., 2017), is characterised by an assembly of uncambered blades positioned symmetrically around a plane perpendicular to the rotational axis. This configuration results in the generation of a unidirectional torque by bidirectional airflow, eliminating the need for rectifying valves. The control of the rotational speed in Wells turbines is driven by the objective of maintaining the turbine's operation close to the optimal efficiency point and alleviating the occurrence of aerodynamic stall on turbine blades. The Wells turbine efficiency characteristic can be represented as follows (Falcão and Gato, 2012):

$$\phi = K_d \psi \tag{17}$$

Up to the best efficiency point, it shows a linear relation between the

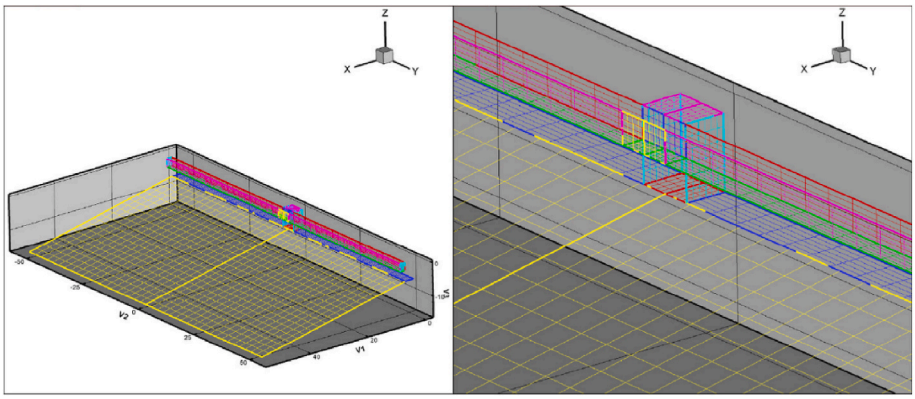

Fig. 5. WAMIT model of Mutriku and detailed view of chamber (Faÿ et al., 2020d).

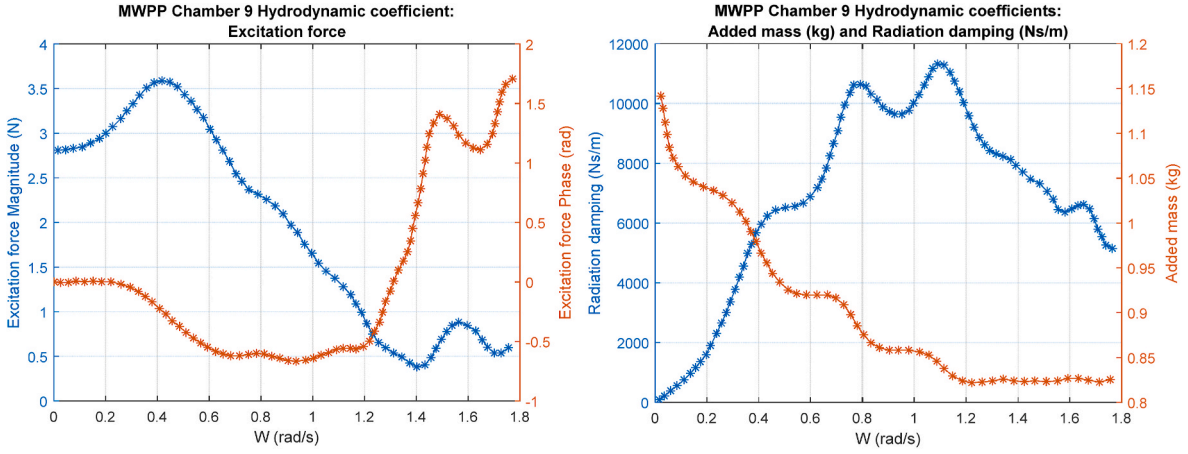

Fig. 6. MWPP Chamber 9, excitation force magnitude(N) and phase (rad), Added mass (kg), radiation damping (Ns/m) (Faÿ et al., 2020d).

normalised (dimensionless) flow rate ϕ and ψ the normalised (dimensionless) pressure, where K_d is a constant that depends on the turbine geometry. Applying dimensional analysis to incompressible flow:

$$\Pi = f_p(\Psi) \tag{18}$$

$$\phi = f_q(\Psi) \tag{19}$$

Where Π dimensionless turbine shaft power, and ψ dimensionless pressure. This can be represented as follows (Falcão and Gato, 2012):

$$\phi = \frac{FR_{turb}}{\rho_{in} W d^3} \tag{20}$$

$$\Pi = \frac{P_{turb}}{\rho_{in} W^3 d^5} \tag{21}$$

$$\psi = \frac{p_c}{\rho_{in} W^2 d^2} \tag{22}$$

Where p_c is the absolute air chamber pressure, q_{turb} the turbine volumetric flow rate at inlet conditions, P_{turb} is the turbine power, FR_{turb} the turbine air flow rate, W the turbine/generator set rotational speed, d is the turbine diameter, and ρ_{in} is the air density at the turbine inlet. Based on the linear relation between flow rate and eqs. (20) and (22), FR_{turb} can be represented as follows:

$$FR_{turb} = p_c \left(k_d d / W \right) \tag{23}$$

The notable decline in the Wells turbine's efficiency stems from blade stall, a phenomenon arising when the angle of attack of the rotor blades amplifies alongside the flow rate. The Wells turbine blades exhibit hard-stall characteristics, imposing an aerodynamic constraint on all control strategies. As well described in (Rosati et al., 2022b), based on eq. (22) preventing stall for substantial pressure heads p_c necessitates an increase in W to ensure that the condition $\Psi < \Psi_{crit}$ is consistently met. Consequently, the rotational speed must surpass a certain threshold defined by:

$$W \geq \sqrt{|p_c| / (\rho_{in} \Psi_{crit} d^2)} \tag{24}$$

Where p_c is the air chamber pressure, d the turbine rotor diameter, Ψ_{crit} the turbine dimensionless pressure head.

This implies that substantial pressure heads require elevated rotational speeds. However, W encounters limitations due to the occurrence of shock waves on the blade's suction surface and the blade stresses resulting from centrifugal forces, which escalate with W^2 (Falcão and Gato, 2012). The blade tip speed velocity is typically capped at $V_{tip} = Wd/2 \leq 180\ m/s$ to prevent shock wave occurrence on the blade's suction surface (Henriques and Gato, 2002). Wells control algorithms should prevent stalls by augmenting rotational speed within the confines of the blade tip speed limit and permissible mechanical stresses. Table 1 presents a summary of the main parameters of the Chamber, Wells turbine.

The Wells turbine has been modelled through dimensionless curves of torque, flow, and pressure jump (Falcão and Rodrigues, 2002). Efficiency curve can be find at (Faÿ et al., 2015), where the biradial, Wells and axial flow impulse turbine efficiencies have been compared Fig. 8 presents the Wells turbine dimensional parameters and optimal

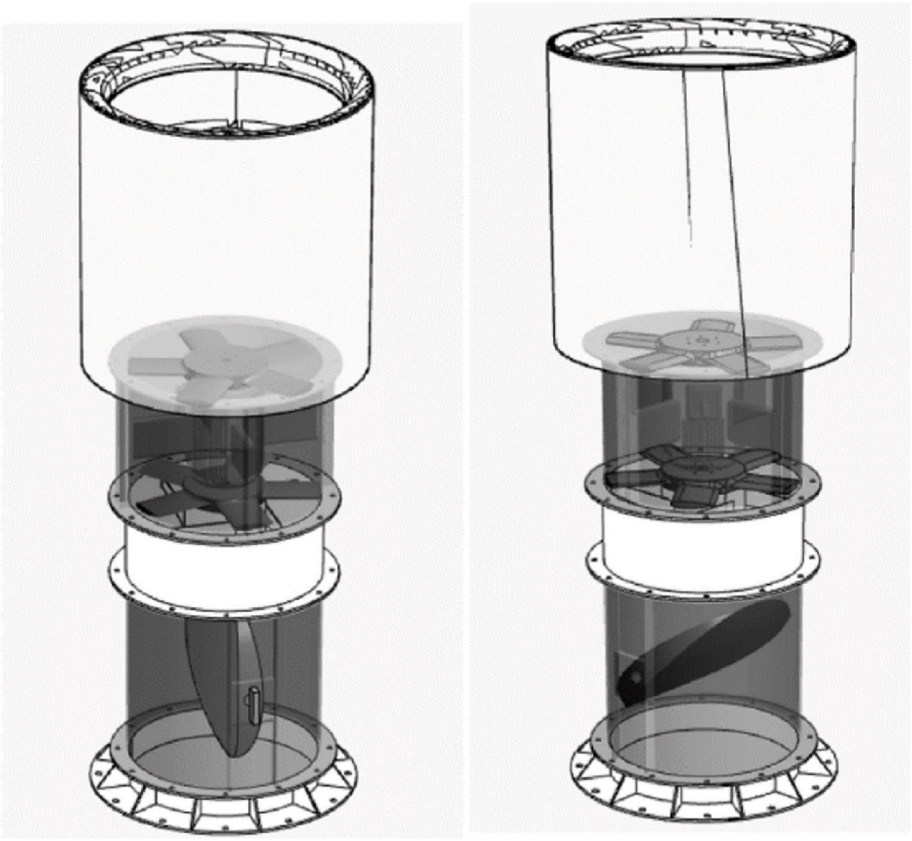

Fig. 7. MWPP PTO; Valve, Wells turbine, and generator. A) valve fully open 90 °, B) valve 45 ° (Ibarra-Berastegi et al., 2021).

Table 1
MWPP Chamber and Wells turbine parameters (Lekube et al., 2018c).

Parameters	Symbol	Value	Unit
w	Chamber width	4.5	m
l	Chamber length	3.1	m
D	Air duct diameter	0.75	m
ρ	Air density	1.19	kg·m^{-3}
b	Blade width	0.21	m
lt	Blade length	0.165	m
n	Number of blades	5	
r	Turbine radius	0.375	m

operation ranges of flow/pressure where the turbine torque is maximum. The pressure is around 10,000–15,000 Pa (blue dash lines) and the flow between 11 and 16 m^3/s (black dash lines).

2.4.2. Damping valve

To date, the pressure measurement in MWPP has only been conducted inside the chamber. However, the turbo-generator configuration in MWPP uses a butterfly-type valve which regulates the airflow that passes through the turbine. At low pressures within the chamber, this valve normally remains fully open (opening angle of 90 °). However, when chamber pressure rms increases to a certain point the control system acts over the valve position thus reducing the opening angle and consequently reducing inlet pressure.

For the present study, a multipurpose flange has been installed, where a pressure sensor (PTX 7500 series (Druck Pressure Sensors)) has been installed to quantify the effect produced by the valve at the inlet of the turbine. The flange has been designed in such a way that it can be easily mounted or disassembled to facilitate its positioning in different places along the turbo-generator column. The height of the flange has been selected to ensure sufficient separation between the

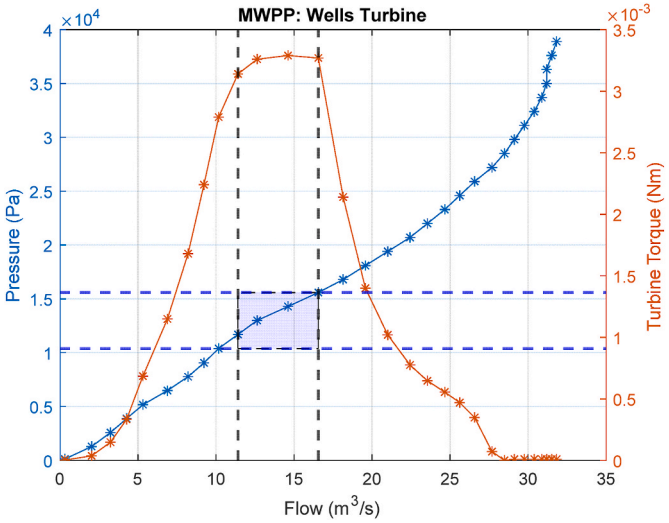

Fig. 8. MWPP: Wells turbine dimensional parameters and optimal operation range.

turbo-generator and sensors, at a minimum separation of half diameter, from any element that might perturb the airflow through the turbine. The flange consists of the following elements that can be seen in Fig. 9: 1. SFB connector 25 E−54/G 1 ¼ ZG, 2. Circular flange, 3. Connection box, 4. Circular joint, 5. Connection box bracket 6. Flange, 7. Cap.

Based on the chamber pressure and inlet pressure sensors, the effect of the valve on the inlet pressure has been characterised. In Fig. 10, one can appreciate the relation experimentally obtained between chamber pressure, inlet pressure, and the angle of the valve.

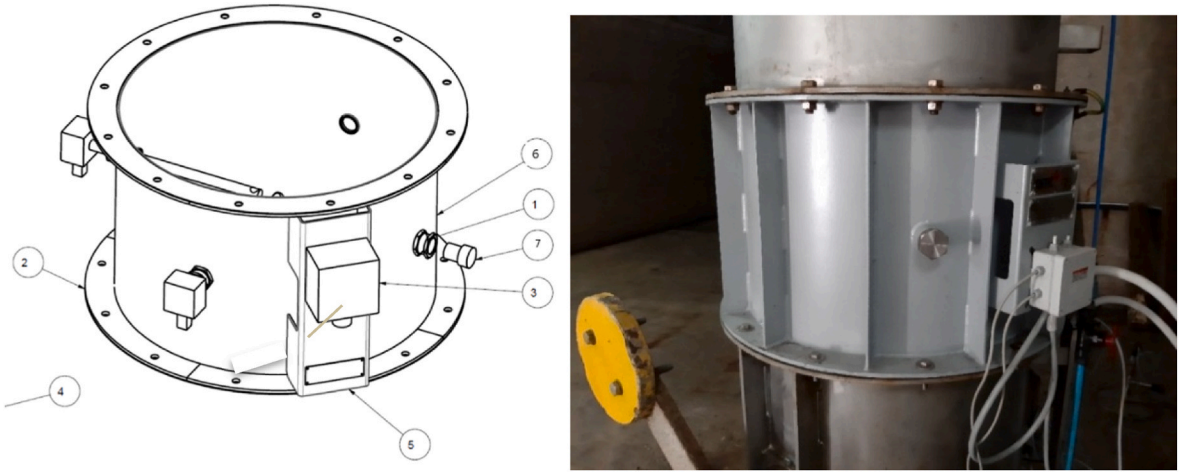

Fig. 9. Parts of the multipurpose flange installed in MWPP.

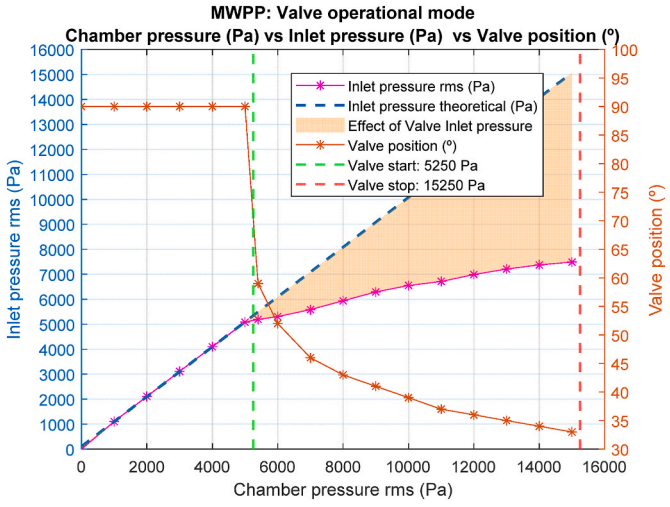

Fig. 10. Relation between the Chamber pressure, damper position, and Inlet pressure.

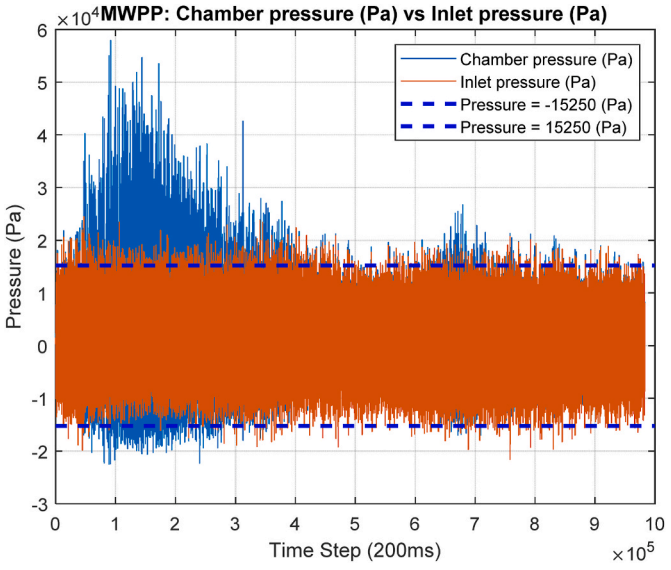

Fig. 11. MWPP: Chamber pressure vs Inlet pressure. Day March 31, 2023 with Hs = 3 m decreasing.

To validate the proper operation ranges at the current control law, the behaviour of the PTO on the day March 31, 2023 has been analysed and shown for illustration in Fig. 11. During this day, severe waves of 3 m Hs were recorded, leading to excessive chamber pressures. As mentioned in previous sections, the valve starts in operation at a dynamic pressure rms of 5250 Pa and stops production at 15,250 Pa. The plot demonstrates that the pressure at the inlet is kept within the range set by the operational limits defined for the activation of the damping valve.

The pressure fluctuates between positive and negative due to the oscillating airflow generated by wave movement. As waves cause the water level in a chamber to rise and fall, the resulting bidirectional airflow is managed by the Wells turbine, which can rotate in the same direction regardless of airflow direction thanks to its symmetrical blades. This oscillating pressure, with air being compressed (positive pressure) when the water level rises and drawn out (negative pressure) when it falls, enables efficient turbine operation.

2.4.3. Generator

A generator control law is used to modify the resisting torque by the generator in function of the turbine rotational speed. Fig. 12 represents the torque/speed relation which has been in operation since the commissioning of the power generation plant. There are three main

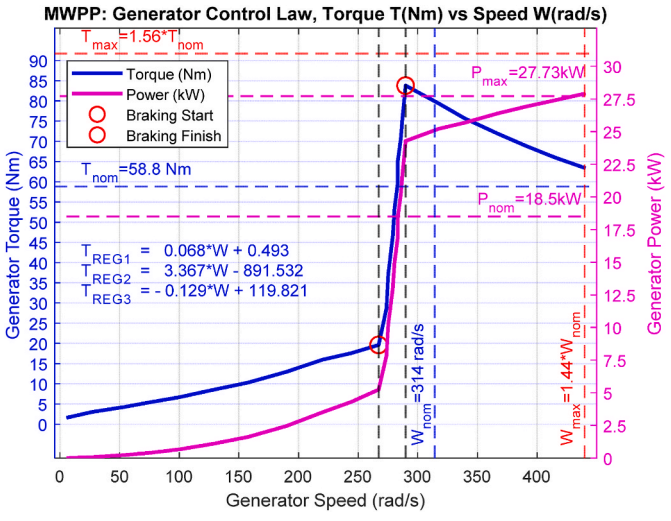

Fig. 12. MWPP Generator Control: Speed (rad/s) vs Torque (Nm).

operation regions. In region 1 ($W \leq 270 rad/s$), the turbine accelerates with a stable relation to torque/speed. Once the rotational speed reaches region 2 ($270 \leq W < 290 rad/s$), the generator begins to apply a larger resisting torque on the PTO, effectively applying a brake and increasing the relation torque/speed until a specified torque limit is reached. Finally, in region 3 ($W \geq 290 rad/s$), the relation torque/speed decreases because the torque cannot be increased above the limit and the generator applies the maximum torque whilst the activation of the damping valve should prevent the rotational speed becoming excessive for the safety of the equipment.

The dynamics of the shaft are represented by the following equation:

$$\dot{W} = \frac{T_T - T_g}{I_T} \tag{25}$$

Where T_T is the aerodynamic torque on the turbine shaft, T_g is the resisting torque exerted by the generator, and I_T is the inertia of the turbine rotor. The efficiency of the generator has been considered based on results obtained in (Lopez-Mendia et al., 2024). For characterising the thermal behaviour of the generator, several sea states have been analysed from MWPP real data to demonstrate that the generator operates below the thermal limit (Generator Stator insulation Class F: $155°C$). Fig. 13 shows the plots of the generator power output and of the stator winding average temperature ($^{\circ}C$) against the chamber pressure rms (Pa).

A thermal model has been utilized to evaluate if the thermal behaviour of the generator at overload, following an increase in its operating limits regarding torque and speed, remains within the insulation limits of the stator winding. For this issue, a first-order model following (Nogal et al., 2021) has been developed. The heat balance equation for the generator has been derived from an idealised system represented by a homogeneous body, where the current and the stator winding resistance are used directly as input:

$$R_u I^2 dt = mcd\theta + S\theta k_p dt \tag{26}$$

Where R_u is the stator winding resistance (Ω), I is the current through the stator windings (A), t the time (s), m the mass of the winding (kg), c is the specific heat of the stator winding ($\frac{J}{kgK}$), θ the temperature (K), S the surface area through which heat is released (m^2) and finally k_p the coefficient of heat transfer from the windings to the ambient ($\frac{W}{Km^2}$).

Equation (26) can be transformed to the final thermal model equation (27) which defines the temperature evolution resulting from a specific power loss directly related to the stator current, considering the previous sample temperature increase (θ_1):

$$\theta_u(t) = \theta_{ss}\left(\frac{I}{I_n}\right)^2\left[1 - e^{-\frac{t}{\tau}}\right] + \theta_{1(t-1)}e^{-\frac{t}{\tau}} \tag{27}$$

Where I corresponds to the instantaneous current, I_n nominal current, θ_{SS} the maximum temperature increase in steady-state, $\tau = 2348.9s$ is adjusted time constant obtained from the cooling curve of the MWPP chamber 2 generator stator temperature presented at Fig. 14.

The numerical model results have been compared with MWPP data (Fig. 15) to evaluate the goodness of the model when it is subject to real conditions and to quantify the sensitivity of the model output to variations in ambient conditions.

Fig. 15 shows the plot of the generator stator winding temperature ($^{\circ}C$) for various chamber pressure RMS values (Pa) comparing the measured values in the MWPP generator in Chamber 2 against those predicted by the numerical model of the thermal behaviour of the generator. This figure shows that the results generated by the numerical model are reasonably representative of the generator stator winding temperatures occurring in reality. The model under study omits four factors that may affect initial conditions: (1) Ambient temperature, which varies significantly throughout the year (1.4 °C–35.6 °C) (Euskalmet Agencia vasca de); (2) Sea water temperature, influencing air-water thermal exchange (15.24 °C–25.53 °C) (Página Inicio puertos); (3) Adiabatic temperature, affected by fluctuating air pressure in the chamber; and (4) Magnetizing temperature, maintained for generator safety to prevent turbine overspeed.

The stator winding temperature is noticeable lower than 155 $^{\circ}C$, which is the maximum allowable operating temperature that generators with Class F insulation (the class of the generators used in MWPP) can withstand in continuous operation (IEEE Recommended Practice for Thermal). Finally, Fig. 16, presents the power production validation of the numerical model vs real measured data at MWPP.

As seen for the generator stator winding temperature, the numerical model predicts the electric power output with reasonable accuracy when compared with the power measured at MWPP.

3. Tuning generator operational limits and damping valve

Several considerations were factored into the design of the MWPP PTO, including operational safety, efficiency, service loads, cost, corrosion resistance, and maintenance accessibility. However, the

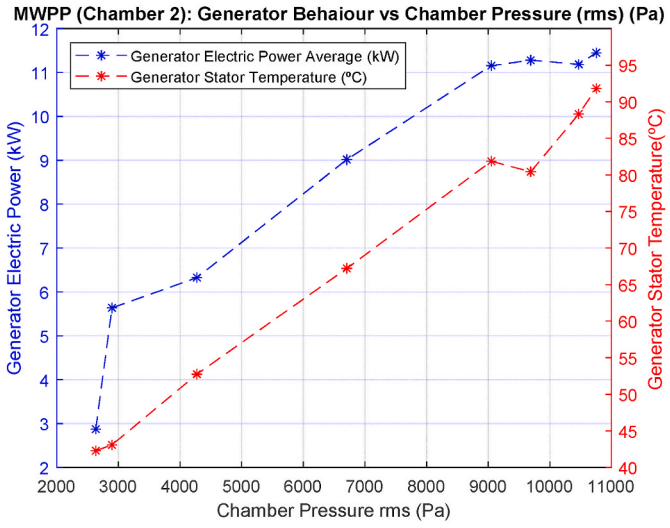

Fig. 13. MWPP chamber 2: generator power output the stator winding average temperature $^{\circ}C$ vs chamber pressure (rms).

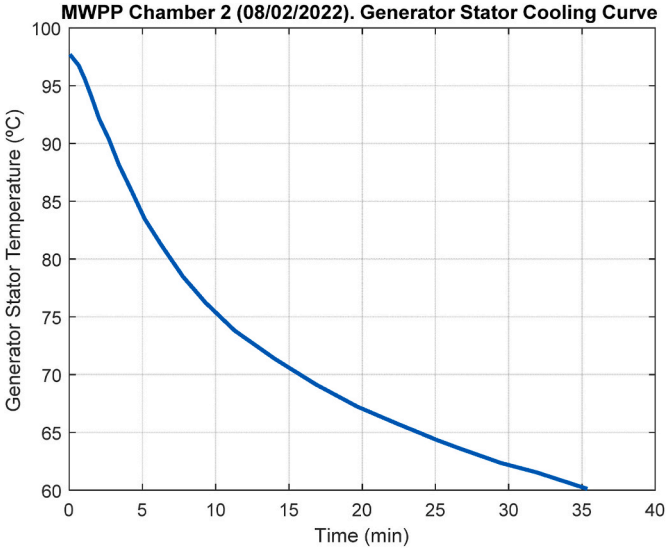

Fig. 14. MWPP chamber 2 (February 08, 2022), Generator Stator Cooling Curve.

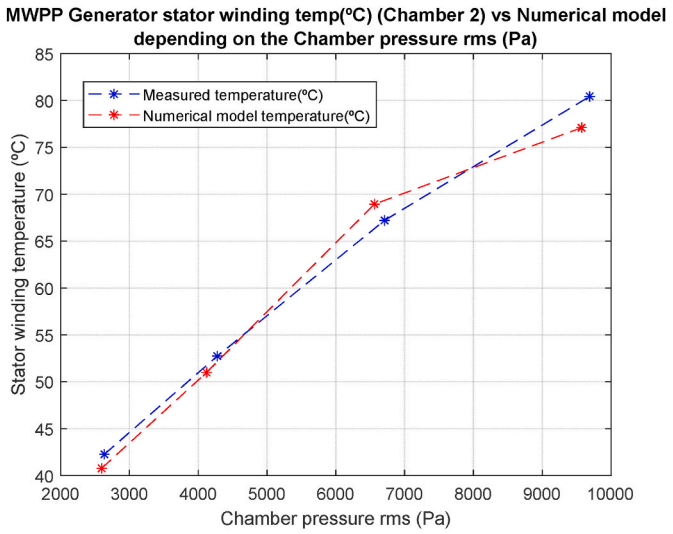

Fig. 15. MWPP Generator stator winding measured temperature ($^{\circ}C$) vs Numerical model temperature depending on the chamber pressure rms (Pa).

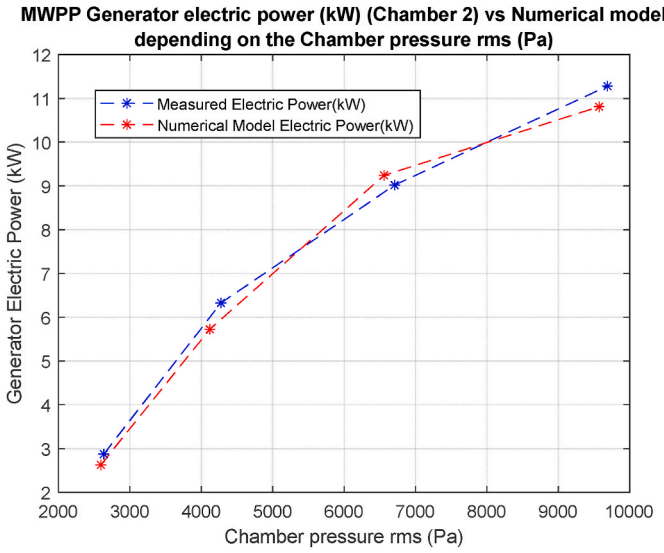

Fig. 16. MWPP Numerical model vs Measured power output comparative.

challenging conditions, characterised by elevated humidity levels and exposure to a saline environment, induce material fatigue that affects the performance of WECs and contributes to the failure of power equipment. The main failures in MWPP reported in (Lekube et al., 2018b)- (M'zoughi et al., 2024) are summarised here.

- Wells Turbine: Exposure to salt water and material fatigue from strong airflows.
- Generator: Exposure to salt water and/or strike by broken blades.
- Bearing cover: Excessive axial force induced in the turbine shaft leads to bearings rubbing against the inside of the generator cover.
- Cooling system: Salt accumulation.

Stator winding failure of the generator is not one of the types of failures and problems reported during the operation of the MWPP. This aligns with the results disclosed in Fig. 15, as the generator's maximum allowable operating temperature is never reached. Consequently, the winding degradation is minimal. Considering this, it seems reasonable to try to increase the generator operating limits to maximize the power extraction. Based on previous studies such as (Lopez-Mendia et al., 2024), where the behaviour of the generator at overload has been studied, the option to increase the torque limit becomes a possibility.

A second element whose modifications could improve the MWPP power production is the damping valve which controls the available pneumatic input power at the turbine. This valve starts operating at chamber pressure rms of 5,250Pa and stops the production at 15,250Pa, with the angle of the valve changing depending on the moving average chamber pressure rms (see Fig. 10).

Based on the Occurrence matrix of MWPP, presented in Figs. 17 and 4 sea states have been selected for the investigation:

Analysing the number of occurrences of significant wave heights and peak period in Mutriku in Fig. 18, it can be observed that 72.9% of the occurrences are between $H_s = 0.25m$ and $H_s = 1.25m$. Under these conditions, an increase in the generator operating limits would have negligible effect and would be useless, so the analysis will focus on sea states with higher waves. Larger waves with height between $H_s = 1.25m$ and $H_s = 3.25m$ account for approximately the 25% of the occurrences, whilst the number of occurrences for waves between $H_s = 3.25m$ and $H_s = 5.25m$ is 2,07%. The most representative periods are between $T_p = 10.5 - 12s$. However, considering that H_s is directly correlated with T_p, a range of $T_p = 12.5$–13s will be selected. Based on this data, four sea states (presented in Table 2) with H_s between 1.5 m and 3 m have been selected for the power production comparative study by modifying generator limits.

3.1. Increasing generator operational limits

Operating the generator above nominal torque (which implies an increase in the generator's temperature) becomes an option to maximize power absorption with optimal efficiency (Kylander, 1995). Table 3 presents the operational limits currently applied to the MWPP generator in its configuration at Mutriku together with the dimensional maximum operational limits set by the manufacturer for the rotational speed W_{CF} and the torque T_{CF}:

Based on the generator limits, Fig. 19 shows the relationship between Wells turbine flow (m^3/s) and mechanical torque ($-$), where CF means capacity factor (being $W_{nom} = 3000rpm$ and $T_{nom} = 58.8Nm$). The following lines are represented:

- Green dashed line represents the present generator torque limit of $T_{CF} = 1.56\ T_{nom}$.
- Blue dashed line represents the generator intermediate maximum torque limit $T_{CF} = 3\ T_{nom}$.
- Red dashed line represents the generator maximum torque limit $T_{CF_{MAX}} = 4.7 T_{nom}$.
- Green continuous line represents the turbine's flow/torque characteristic curve for a maximum rotational speed of $W_{CF} = 1.4 W_{nom}$, which coincides with the current speed limit used in currently at the MWPP.
- Red continuous line represents the turbine relation flow/torque, per generator maximum speed $W_{CF\_MAX} = 2W_{nom}$.
- Finally, the blue continuous line represents the relation flow/torque, for an intermediate generator limit speed of $W_{CF} = 1.7W_{nom}$, where the maximum turbine torque generated is just below the generator torque limit.

Fig. 19 illustrates the potential turbine flow/torque control laws that can be adopted to boost the power production by increasing the operational range of the turbine-generator set whilst avoiding stall effect at the same time. It can be appreciated in the curves how the resultant torque descends drastically for high turbine flows. Increasing speed limits means to increase the stall limit, and therefore increasing generator speed and torque limit means an increment of power production. Three different case studies have been defined in Table 4, with a combination of the maximum speed of the generator of $W_{CF} = 2W_{nom}$, and a

Hs(m)/Tp(s)	0,5	1,5	2,5	3,5	4,5	5,5	6,5	7,5	8,5	9,5	10,5	11,5	12,50	13,5	14,5	15,5	16,5	17,5	18,5	19,5	20,5	21,5	22,5	23,5	24,5
0,25		0,00	0,04	0,50	0,80	0,40	0,30	0,80	1,60	2,00	1,60	1,10	0,70	0,50	0,20	0,10	0,10	0,04	0,06	0,02	0,01	0,01	0,00	0,00	
0,75			0,30	1,90	2,90	1,60	1,80	3,50	6,50	6,60	5,10	3,70	2,60	1,40	0,80	0,70	0,20	0,20	0,09	0,06	0,03	0,02	0,00	0,00
1,25				0,05	0,30	1,00	1,00	1,10	1,80	3,00	3,80	3,60	2,60	1,40	0,90	0,80	0,30	0,20	0,08	0,05	0,02	0,01	0,00	0,00
1,75					0,01	0,10	0,30	0,40	0,50	0,90	1,60	2,30	2,00	1,30	0,70	0,60	0,30	0,10	0,06	0,03	0,02	0,00	0,00	
2,25						0,02	0,09	0,20	0,30	0,40	0,60	1,10	1,50	1,00	0,60	0,50	0,20	0,10	0,05	0,02	0,01	0,00	0,00	
2,75						0,00	0,01	0,07	0,10	0,20	0,30	0,60	0,80	0,80	0,60	0,40	0,20	0,09	0,05	0,01	0,01	0,00	0,00	
3,25							0,00	0,00	0,04	0,07	0,10	0,30	0,40	0,50	0,50	0,50	0,20	0,10	0,04	0,01	0,00	0,00		
3,75								0,00	0,00	0,01	0,04	0,08	0,10	0,20	0,30	0,30	0,20	0,09	0,04	0,01	0,00	0,00		
4,25											0,00	0,01	0,04	0,09	0,09	0,10	0,08	0,07	0,03	0,01	0,00	0,00		
4,75												0,00	0,00	0,01	0,02	0,04	0,02	0,03	0,01	0,00	0,00	0,00		
5,25														0,00	0,00	0,01	0,01	0,01	0,00	0,00				

Fig. 17. MWPP Occurrence matrix.

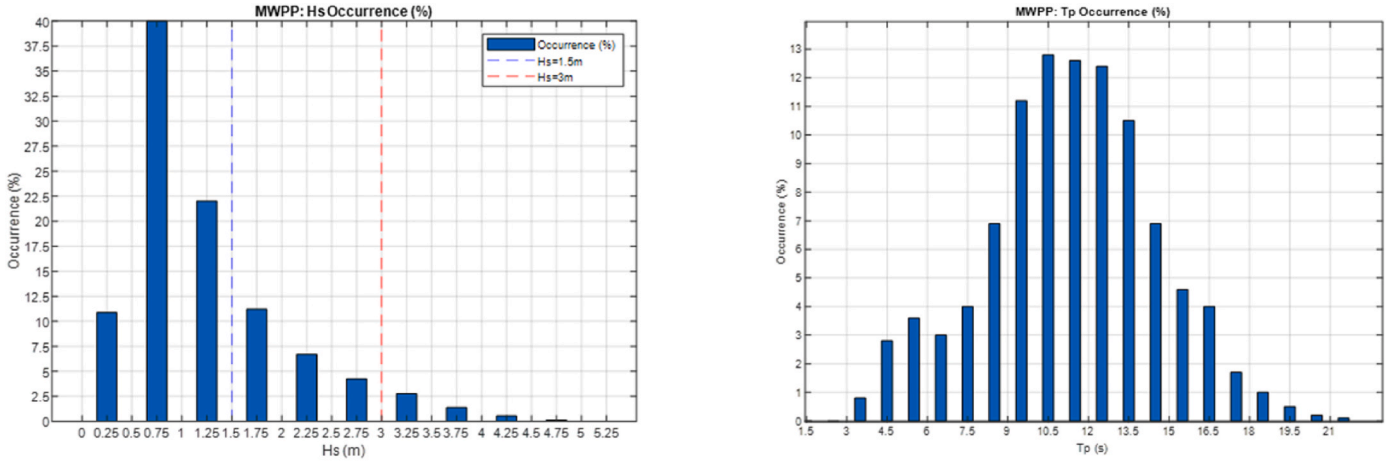

Fig. 18. Mutriku Hs occurrence (%) and Tp occurrence (%).

Table 2
4 Sea states selected properties.

Sea state number	H_s (m)	$T_p(s)$
1	1.5	12.5
2	2.0	12.5
3	2.5	12.5
4	3.0	13.0

Table 3
MWPP generator current and dimensional maximum limits.

	Generator current limits	Generator maximum limits
W_{CF}	$1.4W_{nom}$	$2W_{nom}$
T_{CF}	$1.56\ T_{nom}$	$4.7\ T_{nom}$

maximum torque of $T_{CF} = 3\ T_{nom}$, whose feasibility was demonstrated in a previous study (Lopez-Mendia et al., 2024) by operating the generator at 3 times the nominal torque on a test bench:

Fig. 20 presents the percentage of power production increase for different case studies, measured with respect to the power generated with current limits of $T_{CF} = 1.56\ T_{nom}$ and $W_{CF} = 1.44\ W_{nom}$.

Although the benefit on power production of these changes in the operational limits has been demonstrated, the generator stator insulation thermal behaviour needs to be controlled to ensure that the temperature on the stator winding maintains within the thermal limit. Fig. 21 presents the results of the MWPP generator stator temperature ($°C$) based on the numerical model developed at section 2.4.3 for the 4 sea states and three different generator limits. It can be appreciated that the generator operates inside the stator insulation Class F thermal limits ($155°C$).

It should be noted that, upon analysing the relation between speed and vibrations from (M'zoughi et al., 2024), it appears that there is not a

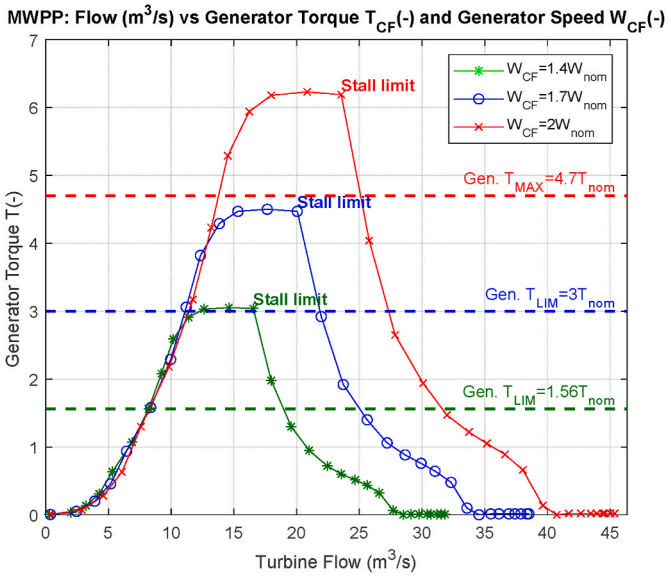

Fig. 19. Wells turbine non-dimensional flow vs torque CF (−) with actual limits and possible available generator limits.

Table 4
MWPP generator case study limits.

	Generator current limits	Option A	Option B	Option C
W_{CF}	$1.44W_{nom}$	$2.00W_{nom}$	$1.44W_{nom}$	$2.00W_{nom}$
T_{CF}	$1.56T_{nom}$	$1.56T_{nom}$	$3.00T_{nom}$	$3.00T_{nom}$

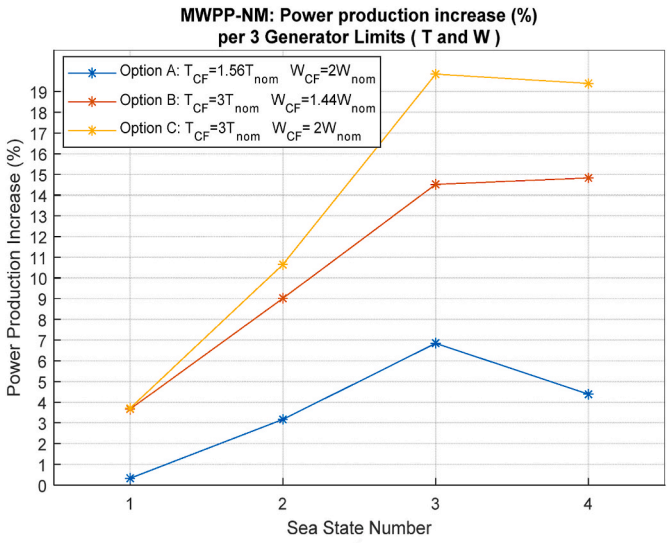

Fig. 20. MWPP numerical model: Power production increase with respect to existing setting (with current limits $T_{CF} = 1.56\ T_{nom}$ and $W_{CF} = 1.44\ W_{nom}$) for several generator limits T_{max} and W_{max}, for 4 sea states.

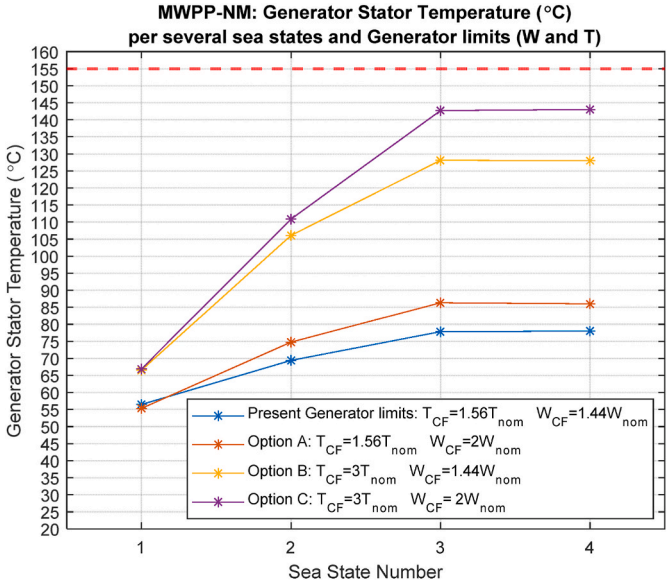

Fig. 21. MWPP Generator stator temperature ($°C$) for 4 sea states and generator limits.

direct correlation between overspeed and increase in vibrations which could cause damage to the PTO. Fig. 22 presents a summary of vibration speed measurements (M'zoughi et al., 2024), plotted against the rotational speed with different colours and symbols depending on the type of operational regime the Wells turbine was working in and the associated problems in the machinery (e.g. unbalanced, problems with the bearing, and occurrence of resonance). The vibration resonance point in MWPP is around 3000 rpm (red points).

Considering this resonance point, the possibility of increasing the generator speed becomes a real option, on one hand, to increase the power output and on the other, to reduce the vibrations on the PTO. Nevertheless, blade tip speed velocity should be analysed, as commented in section 2.4.1, to prevent shock wave occurrence on the blade's suction surface.

3.2. Increasing valve activation point

Analysing the instantaneous pressure data from chamber 2 of the MWPP reveals that the pressure is consistently around 15,000 Pa (Fig. 11). This indicates that the valve operates correctly, limiting the inlet pressure to optimal ranges during energetic sea states and ensuring the PTO generator operates within safe limits.

However, if the RMS pressure activation point is increased, the instantaneous inlet pressure will rise, thereby increasing the average pneumatic power. With the current generator limits, the turbine is more likely to stall. Yet, based on the relationship between the flux and turbine speed presented in equation (24), increasing rotational speed can help maintain the flux within optimal ranges.

This section examines the possibility of raising the valve's operational starting point in conjunction with the generator's operational limits $T_{CF} = 3.0\ T_{nom}$ and $W_{CF} = 2.0\ W_{nom}$. To address this, the four sea states outlined in Table 2 have been analysed for different valve activation starting points (Fig. 23, Fig. 24).

The analysis has not only focused on comparing production relative to the base case with current limits but has also examined the internal behaviour of the generator in terms of thermal response. For this purpose, the thermal model presented in Section 3 has been utilized. In Fig. 23, instances where the thermal limit of class F insulation of the stator winding has been exceeded are marked with a circle. Additionally, Fig. 24 shows the thermal response of the stator winding for each case study. This figure also illustrates both the operating limit and the breakdown limit of the class F insulation for the MWPP generator.

It has been demonstrated how increasing the generator limits in combination with the modification of the damping valve activation point can improve the power production using the same control law.

- For Hs = 1,5 m the valve is not in operation because the chamber pressure rms doesn't increase to 5250 Pa. Nevertheless, an increment of 5% of power can be obtained by increasing the generator limits.
- For sea states of 2 and 2.5 m, an increment of between 10% and 22,5% can be appreciated depending on the valve activation point, with a reasonable thermal response.
- Finally, for the case of 3 m H, the power production increases to between 20% and 38%, but the generator thermal response indicates a degradation of the insulation of the stator winding. At this Hs there is an additional potential problem with the water level, in some cases, rising up to the PTO, inducing non-desirable effects associated with corrosion and splashing of the mechanical and electrical parts.

Once the control limits presented before are validated, the last aspect to be considered before implementing the proposed novel MWPP control limits is their influence on the electrical connection, and the inverter behaviour. The MWPP electrical connection consists of 16 AC/DC drives (Control Techniques Drives Limited, 2008) (Control Techniques Unidrive SP 15 kW Inverter Drive 32 A 380 … 480 V AC Three Phase) which are connected through a DC bus to DC/AC inverter, and then throughout 0.460kV/13,2 kV Merlin Gerin transformer the energy is delivered to the grid. The Unidrive Inverter has a thermal limitation of 110 $°C$, in addition to the reduced rated power, and this is possibly the main bottleneck element within the power train. A deeper analysis should be completed to understand the thermal behaviour of the converter when the generator operating limits are increased. In any case, the increase in captured power would more than justify selecting a larger power conversion stage if necessary. This makes the proposed option of increasing the maximum operating ranges of the generator and the valve a promising choice for boosting power production.

4. Conclusions

The study demonstrated that sensors installed in the MWPP provided valuable insights into the operation of the PTO system. By using a

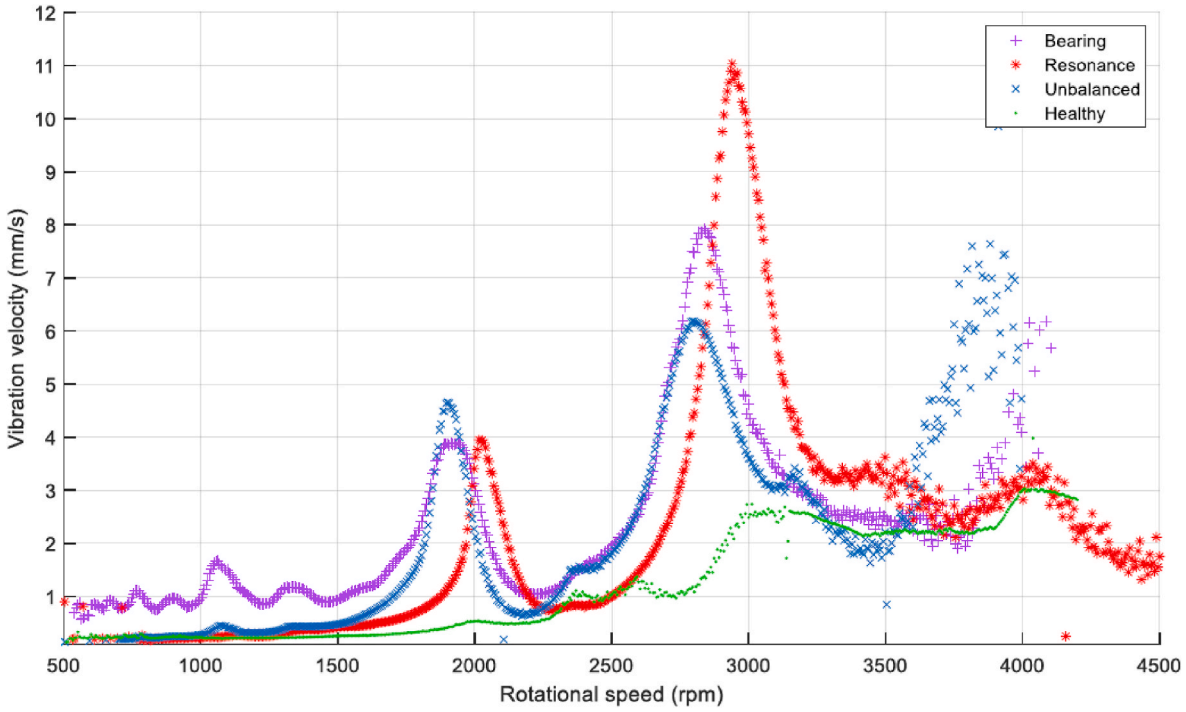

Fig. 22. Vibrations velocity for several cases: Healthy Wells turbine, unbalanced turbine, bearing problems, and resonance problems (M'zoughi et al., 2024).

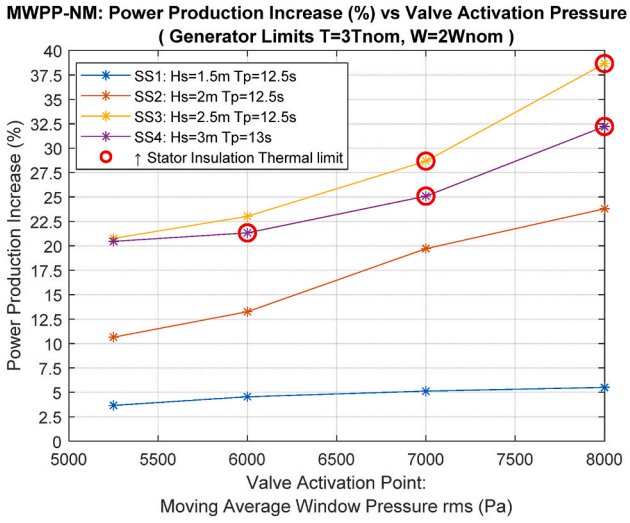

Fig. 23. MWPP-NM: Summary of Power production increment (%) increasing generator Limits (T and W) and for several valve activation points.

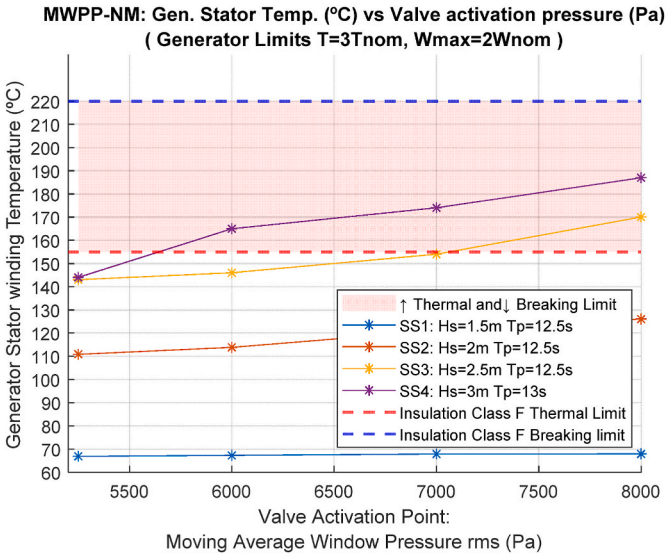

Fig. 24. Generator stator temperature ($^{\circ}C$) vs Valve activation rms pressure for several sea states.

calibrated numerical model (MWPP-NM), it was shown that increasing the generator's operational limits, torque and speed, can enhance power production while keeping the thermal response within safe limits (below $155^{\circ}C$).

The MWPP-NM helped explore power production gains under various sea states by adjusting generator and valve settings. For sea states with wave heights $H_s < 2.0m$, the damping valve was inactive, but power increases of up to 5% were observed with adjusted generator limits for $H_s = 1.5m$. For higher sea states $H_s = 2 - 2.5m$, power increases ranged from 10% to 30%, depending on valve activation points. In very energetic sea states $H_s \geq 3m$, while power production rose, the thermal response indicated potential risks of stator insulation damage and other operational issues, such as water intrusion into the PTO. Future work may explore hybrid strategies to maximize performance under these conditions.

Additionally, the thermal model for the generator's stator winding was validated and showed accurate temperature predictions. However, the study also highlighted limitations, as the thermal model is sensitive to environmental factors like ambient temperature and air pressure, which affect the cooling effect of the airflow in Oscillating Water Column (OWC) systems. These factors should be incorporated in future studies to refine the model's accuracy.

Future research will focus on analyzing the thermal behaviour of the power converter to prevent overheating and applying the knowledge gained in full-scale tests of OWC systems, including ongoing projects like the TurboWave initiative [63].

CRediT authorship contribution statement

Joseba Lopez-Mendia: Writing – review & editing, Writing – original draft, Validation, Software, Methodology, Investigation, Formal analysis, Data curation, Conceptualization. **Ander Aristondo:** Writing – review & editing, Validation, Software. **Pierpaolo Ricci:** Writing – review & editing, Validation. **Jon Lekube:** Writing – review & editing, Software, Investigation, Data curation. **Salvador Ceballos:** Writing – review & editing, Writing – original draft, Supervision, Methodology. **Eider Robles:** Writing – review & editing, Project administration, Funding acquisition, Conceptualization.

Declaration of competing interest

The authors declare that they have no known competing financial interests or personal relationships that could have appeared to influence the work reported in this paper.

Acknowledgments

The research has been carried out within the framework of the VALID project and received funding from the European Union's Horizon 2020 research and innovation program under Grant Agreement No 101006927.

References

Características técnicas – BiMEP, (n.d.). https://www.bimep.com/area-mutriku/caracteristicas-tecnicas/(accessed July 5, 2024).
Carrelhas, A.A.D., Gato, L.M.C., Henriques, J.C.C., 2023. Peak shaving control in OWC wave energy converters: from concept to implementation in the Mutriku wave power plant. Renew. Sustain. Energy Rev. 180, 113299. https://doi.org/10.1016/j.rser.2023.113299.
Control Techniques drives limited, user guide unidrive, model sizes 0 to 6. Universal variable speed AC drive for induction and servo motors. www.controltechniques.com, 2008.
Druck Pressure Sensors/Pressure Calibrators Baker Hughes, (n.d.). https://www.bakerhughes.com/druck (accessed March 2, 2024).
Duclos, G., Clément, A.H., Chatry, G., 2001. Absorption of outgoing waves in a numerical wave tank using a self-adaptive boundary condition. Int. J. Offshore Polar Eng. 11.
Euskalmet Agencia vasca de meteorología, (n.d.). https://www.euskalmet.euskadi.eus/inicio/(accessed May 4, 2024).
Falcão, A.F.O., Gato, L.M.C., 2012. Air turbines. In: Comprehensive Renewable Energy. Elsevier, pp. 111–149. https://doi.org/10.1016/B978-0-08-087872-0.00805-2.
Falcão, A.F.O., Henriques, J.C.C., 2016. Oscillating-water-column wave energy converters and air turbines: a review. Renew. Energy 85, 1391–1424. https://doi.org/10.1016/j.renene.2015.07.086.
Falcão, A.F. de O., Rodrigues, R.J.A., 2002. Stochastic modelling of OWC wave power plant performance. Appl. Ocean Res. 24, 59–71. https://doi.org/10.1016/S0141-1187(02)00022-6.
Falcão, A.F.O., Sarmento, A.J.N.A., Gato, L.M.C., Brito-Melo, A., 2020. The Pico OWC wave power plant: its lifetime from conception to closure 1986–2018. Appl. Ocean Res. 98, 102104. https://doi.org/10.1016/j.apor.2020.102104.
Faÿ, X.-F., Henriques, J.C.C., Marcos, M., Robles, E., 2015. Review of Control Strategies for Oscillating Water Column Wave Energy Converters. Nantes, France.
Faÿ, F.-X., Robles, E., Marcos, M., Aldaiturriaga, E., Camacho, E.F., 2020a. Sea trial results of a predictive algorithm at the Mutriku Wave power plant and controllers assessment based on a detailed plant model. Renew. Energy 146, 1725–1745. https://doi.org/10.1016/j.renene.2019.07.129.
Faÿ, F.-X., Henriques, J.C., Kelly, J., Mueller, M., Abusara, M., Sheng, W., Marcos, M., 2020b. Comparative assessment of control strategies for the biradial turbine in the Mutriku OWC plant. Renew. Energy 146, 2766–2784. https://doi.org/10.1016/j.renene.2019.08.074.
Faÿ, F.-X., Robles, E., Marcos, M., Aldaiturriaga, E., Camacho, E.F., 2020c. Sea trial results of a predictive algorithm at the Mutriku Wave power plant and controllers assessment based on a detailed plant model. Renew. Energy 146, 1725–1745. https://doi.org/10.1016/j.renene.2019.07.129.
Faÿ, F.-X., Robles, E., Marcos, M., Aldaiturriaga, E., Camacho, E.F., 2020d. Sea trial results of a predictive algorithm at the Mutriku Wave power plant and controllers assessment based on a detailed plant model. Renew. Energy 146, 1725–1745. https://doi.org/10.1016/j.renene.2019.07.129.
Fox, B.N., Gomes, R.P.F., Gato, L.M.C., 2021. Analysis of oscillating-water-column wave energy converter configurations for integration into caisson breakwaters. Appl. Energy 295, 117023. https://doi.org/10.1016/j.apenergy.2021.117023.
Gato, L.M.C., Henriques, J.C.C., Carrelhas, A.A.D., 2022. Sea trial results of the biradial and Wells turbines at Mutriku wave power plant. Energy Convers. Manag. 268, 115936. https://doi.org/10.1016/j.enconman.2022.115936.
Heath, T.V., 2000. The development and installation of the Limpet wave energy converter. In: World Renewable Energy Congress VI. Elsevier, pp. 1619–1622. https://doi.org/10.1016/B978-008043865-8/50334-2.
Henriques, J.C.C., Gato, L.M.C., 2002. Use of a residual distribution Euler solver to study the occurrence of transonic flow in Wells turbine rotor blades. Comput. Mech. 29, 243–253. https://doi.org/10.1007/s00466-002-0337-8.
Home - EVE, (n.d.). https://www.eve.eus/?lang=en-gb (accessed March 3, 2024).
Home - OPERA H2020, (n.d.). https://opera-h2020.eu/(accessed March 2, 2024).
Ibarra-Berastegi, G., Ulazia, A., Sáenz, J., Serras, P., González Rojí, S.J., Esnaola, G., Iglesias, G., 2021. The power flow and the wave energy flux at an operational wave farm: findings from Mutriku, Bay of Biscay. Ocean. Eng. 227, 108654. https://doi.org/10.1016/j.oceaneng.2021.108654.
IEEE Recommended Practice for Thermal Evaluation of Insulation Systems for AC Electric Machinery Employing Form-Wound Pre-Insulated Stator Coils, Machines Rated 6900 V and Below, IEEE, n.d. https://doi.org/10.1109/IEEESTD.1981.7394908.
Kylander, G., 1995. Thermal Modelling of Small Cage Induction Motors. Chalmers University of Technology.
Lekube, J., Garrido, A.J., Garrido, I., 2018a. Variable speed control in wells turbine-based oscillating water column devices: optimum rotational speed. IOP Conf. Ser. Earth Environ. Sci. 136, 012017. https://doi.org/10.1088/1755-1315/136/1/012017.
Lekube, J., Ajuria, O., Ibeas, M., Igareta, I., Gonzalez, A., 2018b. Fatigue and aerodynamic loss in wells turbines: Mutriku wave power plant case. In: 7th International Conference on Ocean Energy. Cherbourg, France.
Lekube, J., Garrido, A., Garrido, I., Otaola, E., Maseda, J., 2018c. Flow control in wells turbines for harnessing maximum wave power. Sensors 18, 535. https://doi.org/10.3390/s18020535.
J. Lopez-Mendia, E. Robles, S. Ceballos, P. Ruiz-Minguela, J. Rotger, Improving the OWC wave energy converter power take-off efficiency throughout experimental and numerical characterisation of an SCIG, Energies 2024, 17(5), 1146; Https://Doi.Org/10.3390/En17051146 (n.d.).
Mutriku Wave Energy Plant hits new output milestone, generating 2 GWh - EVE, (n.d.). https://www.eve.eus/Jornadas-y-Noticias/Noticias/La-planta-de-energia-de-las-olas-de-Mutriku-bate?lang=en-gb (accessed March 2, 2024).
M'zoughi, F., Lekube, J., Garrido, A.J., De La Sen, M., Garrido, I., 2024. Machine learning-based diagnosis in wave power plants for cost reduction using real measured experimental data: Mutriku Wave Power Plant. Ocean. Eng. 293, 116619. https://doi.org/10.1016/j.oceaneng.2023.116619.
Nereida MOWC: OWC integration in the new mutriku breakwater | NEREIDA MOWC Project | Fact Sheet | FP6, CORDIS | European Commission (n.d.). https://cordis.europa.eu/project/id/38521 (accessed March 3, 2024).
Nogal, Ł., Magdziarz, A., Rasolomampionona, D.D., Łukaszewski, P., Sapuła, Ł., Szreder, R., 2021. The laboratory analysis of the thermal processes occurring in low-voltage asynchronous electric motors. Energies 14. https://doi.org/10.3390/en14082056, 2056.
Página Inicio puertos.es, (n.d.). https://www.puertos.es/es-es (accessed May 4, 2024).
Perez, T., Fossen, T.I., 2009. A matlab toolbox for parametric identification of radiation-force models of ships and offshore structures. Model. Ident. Control 30, 1–15. https://doi.org/10.4173/mic.2009.1.1.
Raghunathan, S., Tan, C.P., Wells, N.A.J., 1982. Theory and performance of a Wells turbine. J. Energy 6, 157–160. https://doi.org/10.2514/3.48047.
Rosati, M., Henriques, J.C.C., Ringwood, J.V., 2022a. Oscillating-water-column wave energy converters: a critical review of numerical modelling and control. Energy Convers. Manag. X 16, 100322. https://doi.org/10.1016/j.ecmx.2022.100322.
Rosati, M., Henriques, J.C.C., Ringwood, J.V., 2022b. Oscillating-water-column wave energy converters: a critical review of numerical modelling and control. Energy Convers. Manag. X 16, 100322. https://doi.org/10.1016/j.ecmx.2022.100322.
Scialò, A., Henriques, J.C.C., Malara, G., Falcão, A.F.O., Gato, L.M.C., Arena, F., 2021. Power take-off selection for a fixed U-OWC wave power plant in the Mediterranean Sea: the case of Roccella Jonica. Energy 215, 119085. https://doi.org/10.1016/j.energy.2020.119085.
Shehata, A.S., Xiao, Q., Saqr, K.M., Alexander, D., 2017. Wells turbine for wave energy conversion: a review: wells turbine for wave energy conversion: a review. Int. J. Energy Res. 41, 6–38. https://doi.org/10.1002/er.3583.
Technical Characteristics – BiMEP, (n.d.). https://www.bimep.com/en/mutriku-area/technical-characteristics/(accessed March 1, 2024).
The Mutriku wave plant achieves cumulative electricity production of three million kilowatts per hour – BiMEP, (n.d.). https://www.bimep.com/en/the-mutriku-wave-plant-achieves-cumulative-electricity-production-of-three-million-kilowatts-per-hour/(accessed March 2, 2024).
Torre-Enciso, Y., et al., 2009. Mutriku wave power plant: from the thinking out to the reality. In: Proceedings of the 8th European Wave and Tidal Energy Conference, pp. 319–329. Uppsala, Sweden.
Touzon, I., de Miguel, B., Nava, V., Petuya, V., Mendikoa, I., Boscolo, F., 2018. Mooring System Design Approach: A Case Study for MARMOK-A Floating OWC Wave Energy Converter. American Society of Mechanical Engineers Digital Collection. https://doi.org/10.1115/OMAE2018-77634.
Wave Swell, (n.d.). https://www.waveswell.com/(accessed July 2, 2024).

Weber, J., 2007. Representation of non-linear aero-thermodynamic effects during small scale physical modelling of OWC WECs. In: Proceedings of the 7th European Wave and Tidal Energy Conference. Porto, Portugal.

WEDUSEA wave energy project, WEDUSEA (n.d.). https://wedusea.eu/wave-energy/our-wave-energy-technology/(accessed February 7, 2024).

Xu, C., Huang, Z., 2018. A dual-functional wave-power plant for wave-energy extraction and shore protection: a wave-flume study. Appl. Energy 229, 963–976. https://doi.org/10.1016/j.apenergy.2018.08.005.